Hybrid Advances 9 (2025) 100420

Contents lists available at ScienceDirect

Hybrid Advances

journal homepage: www.journals.elsevier.com/hybrid-advances

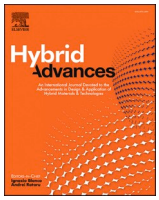

Research Article

# Efficient methylene blue dye degradation via visible light-activated g-$C_3N_4$/CuO nanocomposites

A. Muthuganesh [a,g], S. Mohamed Rafi [b], I. Davis Jacob [c], J.P. Soundranayagam [d], S. Surender [e,f], P. Elangovan [b], X. Helan Flora [a,g,*]

[a] Department of Physics, Kamaraj College, Tuticorin, 628003, India
[b] PG & Research Dept. of Physics, Pachaiyappa's College, Chennai, 600 030, India
[c] Department of Science and Humanities, JP College of Engineering, Ayikudi, Tenkasi, 627852, India
[d] Centre for Scientific and Applied Research, V. O. Chidambaram College, Tuticorin, 628008, India
[e] Department of Physics, Saveetha School of Engineering, Saveetha Institute of Medical and Technical Sciences (SIMATS), Chennai, 602 105, India
[f] School of Engineering, Cardiff University, Cardiff, UK
[g] Affiliated to Manonmanium Sundaranar University, Abishekapatti, Tirunelvelli, 627012, Tamil Nadu, India

ARTICLE INFO

*Keywords:*
Graphitic g-$C_3N_4$
Coper oxide
Degradation
Photo-generated electrons
Photocatalytic behaviour

ABSTRACT

In this work, pure and heterostructured g-$C_3N_4$/CuO photocatalyst materials were prepared using a combination of thermal decomposition and hydrothermal techniques. The phase and purity of the catalysts were examined using powder X-ray diffraction (XRD). The prepared catalysts were also assessed using different systematic techniques, which demonstrated that the addition of CuO to the g-$C_3N_4$ matrix significantly altered the particle size, crystallinity, morphology, and energy bandgap. Heterojunction formation and interfacial contact between CuO and g-$C_3N_4$were confirmed by TEM and XPS analyses. The photocatalytic activity of the g-$C_3N_4$/CuO nanocomposite was assessed by its ability to break down Methylene Blue (MB), an organic contaminant, under visible-light exposure. Remarkably, the g-$C_3N_4$/CuO catalyst demonstrated rapid photocatalytic degradation of MB, achieving 98 % breakdown within 40 min. The increased degradation efficiency of g-$C_3N_4$/CuO is due to its lower energy bandgap, enhanced charge transport, and lower charge recombination compared to pure CuO and g-$C_3N_4$. Therefore, constructing a g-$C_3N_4$/CuO heterostructure could be a promising technique for sewer water treatment.

## 1. Introduction

Environmental pollutants and synthetic dyes are frequently used in a variety of sectors. Their excessive use can lead to an unwanted and hazardous occurrence whereby these dyes are released into aquatic reservoirs as industrial effluents [1]. These dyes are frequently used as colouring agents in paper, paint, food, textile, pharmaceutical, and leather industries. The introduction of these carcinogenic azo dyes into the aquatic environment results in adverse structural alterations to the ecosystem. These dyes produce hypertrophication, which severely harms aquatic flora and fauna and lowers marine life's ability to absorb oxygen. Since humans eat aquatic food, humans are also indirectly impacted by the bioaccumulation and biomagnification of these hazardous dyes in the aquatic environment. Methylene blue (MB) is a well-known, highly carcinogenic thiazine pollutant that has been produced and utilized for a variety of reasons in numerous sectors, including hair colouring, paper colouring, and the dying of cotton, wool, and textiles [2]. MB poses a major risk to human health when consumed and has been linked to neurological and ocular impairment. Other related illnesses include gastritis infections, nausea, vomiting, diarrhoea, and respiratory problems. Consequently, it is crucial to create such cutting-edge tactics that can remove such dangerous toxins from water bodies. There are several reported removal techniques that can efficiently break down these harmful pollutants in the aqueous medium in order to solve this environmental problem. A few of these removal techniques are photo-oxidation [3], ion-exchange removal [4], membrane filtration [5], adsorption [6], biological therapies [7], and photocatalytic degradation [8,9]. Compared to alternative techniques, photocatalytic pollution removal has several advantages, such as the use of a renewable resource (sunlight), a simple operating scheme, effective

* Corresponding author. Department of Physics, Kamaraj College, Tuticorin, 628003, India.
*E-mail address:* helanfloraphy@gmail.com (X.H. Flora).

https://doi.org/10.1016/j.hybadv.2025.100420
Received 9 December 2024; Received in revised form 4 February 2025; Accepted 18 February 2025
Available online 20 February 2025

dye removal and complete mineralization, etc. Semiconductor photocatalyst converts solar energy into chemical energy, which degrades the pollutant under sunlight irradiation [10]. In recent years, emerging technologies such as piezoelectric and piezo-photocatalysis have also gained traction for environmental remediation. Piezo-photocatalysis integrates the piezoelectric effect with photocatalysis, enhancing charge separation under mechanical stress combined with light irradiation. This innovative approach enables the generation of reactive species through piezoelectric polarization charges, improving the degradation efficiency of organic pollutants. For example, studies have shown that piezoelectric materials like ZnO and BaTiO3 [11–14] exhibit significant potential for synergistic dye degradation. Recent works, including the development of novel piezo-photocatalysts [15], detailed reviews on piezoelectric materials [16], and applications in environmental management [17], underscore the relevance of this approach.

Although piezo-photocatalysis represents a promising direction, photocatalytic techniques using heterostructured materials, such as g-C3N4/CuO, remain highly effective for dye degradation under visible light irradiation. Compared with above mentioned materials the graphitic carbon nitride (g-$C_3N_4$) has lot of properties such as two-dimensional (2D) nanostructure, narrow band gap energy (2.7 eV), high charge separation and high chemical stability have attracted tremendous attention for the research [18]. Due to its low cost, superior durability, and nontoxicity, graphitic carbon nitride assisted photocatalysis is becoming more and more popular. However, the g-$C_3N_4$ band gap and valance band potential result in a limited oxidation ability and quick recombination of photo-generated charge carriers resulting low photocatalytic degradation performance [19–21]. Therefore, g-C3N4 with other adequate band position can be changed with other semiconductors to generate a heterostructure. In the interest of increasing photocatalytic activity, a numerous approaches have been explored such as doping, construction of heterostructures and coupling with metal or non-metal semiconductors. In the field of photocatalytic activities, there has been a notable advancement in the use and development of metal oxide materials at the nanoscale level in recent years. Copper oxide, nickel oxide, tungsten oxide, manganese oxide, and ruthenium oxide are some of the most often used metal oxides [22–29]. CuO is one among them and has drawn a lot of interest due to its economic viability, abundance of resources, excellent catalytic performance, and commitment to the environment. During the recent years, the photocatalytic degradation performance of various organic pollutants have been investigated by g-C3N4 based materials such as CuO/NiO [30], CuO/$TiO_2$ [31], CuO/Ag [32], CuO/ZnO [33]. The synthesis of CuO/g-C3N4 was achieved through a combination of thermal decomposition and hydrothermal techniques. This approach not only ensures high interfacial contact between CuO and g-C3N4 but also optimizes the structural and optical properties of the composite, leading to superior photocatalytic performance. By exposing MB aqueous to visible light, the synthesized materials' photocatalytic activity was also investigated. Comparing the g-$C_3N_4$/CuO nanocomposite to two pure g-$C_3N_4$ and CuO samples, the former exhibits increased photocatalytic activity. To better understand the optical response mechanism, the improvement of photocatalytic performance was carefully explored. Researchers trying to create environmentally and economically sound materials with high dye degradation efficiency will find this work to be a great resource. The research offers detailed analysis of the charge transfer dynamics and the photocatalytic mechanism. Advanced characterization techniques, including XPS and TEM, confirm the formation of a robust heterojunction, which enhances the separation of photogenerated electrons and holes, reducing charge recombination. Overall, the study extensively evaluated the structural stability and reusability of the photocatalyst over multiple cycles, highlighting its practicality for large-scale applications. These aspects collectively contribute to the advancement of CuO/g-C3N4 photocatalysts, offering practical environmental remediation solutions while addressing the limitations of existing methods.

## 2. Materials and methods

The source of $C_3N_4$ material is melamine, which was purchased from sigma aldrich (99 %). Trapping test were carried out with the following chemicals $AgNO_3$, EDTA, isopropanol IPA, p-benzoquinone (BQ), Methylene Blue (MB). The chemicals used for the experiments are analytical grades with negligible purification.

### 2.1. Fabrication of g-$C_3N_4$/CuO photocatalysts

Initially, 3g of melamine was heated to 550 °C for 3 h by ramping the temperature up by 3 °C/min to create g-$C_3N_4$ using the thermal breakdown method. The final g-$C_3N_4$ product had a yellowish tint and was finely powdered. Using the same thermal decomposition technique, more copper oxide was produced from copper acetate monohydrate. The required quantity of source material was placed in an alumina crucible and subjected to a 3-h heat treatment in a muffle furnace, maintaining a consistent temperature and ramping rate. To create the nanocomposite substance, the appropriate amounts of g-$C_3N_4$ and 3 wt percent of CuO were mixed in 75 ml of distilled water and stirred for an hour. Subsequently, the homogeneous solution was introduced into a Teflon-lined autoclave and underwent hydrothermal treatment for 4 h at 180 °C (Fig. 1). Following the hydrothermal process, the resulting product underwent thorough cleaning and drying in a vacuum oven before being utilized in further tests and characterization.

### 2.2. Characterization

The crystalline structure of the synthesized photocatalysts was analyzed using a Bruker D8 Advance diffractometer equipped with Cu Kα radiation (λ = 1.5406 Å), operating at 40 kV and 30 mA. The diffraction patterns were recorded in the 2θ range of 10°–60°, with a step size of 0.02° and scan speed of 1°/min. FE-SEM: High-resolution imaging was performed using a FEI Quanta 200 (Netherlands) Field Emission Scanning Electron Microscope at an accelerating voltage of 5–15 kV, with gold sputtering applied to improve conductivity. High-resolution TEM imaging was carried out using a JEOL JEM-2100F microscope operating at 200 kV, providing insights into the microstructural features of the nanocomposite. The functional groups of the synthesized catalysts were examined using an FTIR spectrometer (Bruker Tensor 27) in the range of 500–2000 $cm^{-1}$ with a resolution of 4 $cm^{-1}$. The spectra were collected using the KBr pellet technique. Optical properties and band gap determination were conducted using a Shimadzu UV-3600 spectrophotometer equipped with an integrating sphere attachment, with $BaSO_4$ as the reference. The recombination behavior of photogenerated charge carriers was studied using a Horiba Fluoromax-4 spectrofluorometer with an excitation wavelength of 320 nm. The electron transfer resistance was analyzed using a CHI660E electrochemical workstation in a three-electrode system with an Ag/AgCl reference electrode, a platinum counter electrode, and a working electrode prepared by drop-casting the photocatalyst onto an FTO substrate. The measurements were performed in 0.1 M $Na_2SO_4$ electrolyte solution with an AC amplitude of 10 mV over the frequency range of 0.1 Hz–1 MHz. The surface charge of the prepared photocatalysts was evaluated using a Malvern Zetasizer Nano ZS (ZEN3600) at room temperature, with measurements taken at a pH range of 3–11 to determine the isoelectric point (pH_IEP).

### 2.3. Photocatalytic measurements

Using an Annular type photoreactor, dye MB in aqueous solution was broken down to conduct photocatalytic tests. The source of visible light irradiation was a 400W halogen lamp. The photocatalyst sample (100 mg) and MB (5 mgL1, 100 mL) were agitated in the dark for 30 min to achieve the adsorption-desorption equilibrium condition between the MB molecules and the produced photocatalyst. Every 10 min during the

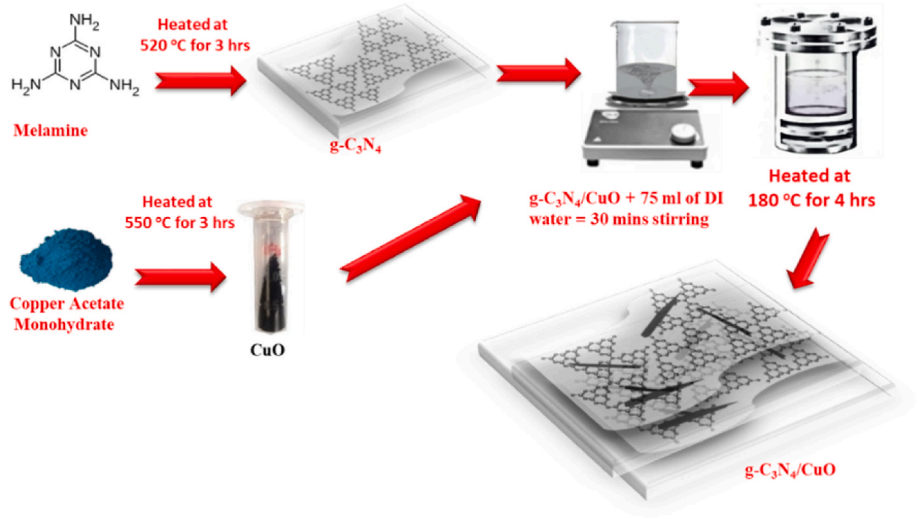


**Fig. 1.** Schematic diagram of the synthesis process for g-$C_3N_4$/CuO nanocomposite.

irradiation procedure, 4 mL aliquots were taken and centrifuged for 15 min to remove any suspended g-$C_3N_4$/CuO photocatalyst particles. Additionally, the concentration of the supernatant solution was examined using a UV–vis spectrophotometer.

In order to gain a comprehensive understanding of the photocatalytic mechanism, the influence of various active species on the degradation of the MB solution was systematically examined. Typically, a specific quantity of photocatalyst was dispersed in a solution containing methylene blue (MB) alongside specific quenchers, including EDTA-2Na (18.61 mg, a quencher of h+), IPA (10 % by volume, a quencher of •OH), BQ (5.4 mg, a quencher of O2-), and $AgNO_3$ (8.45 mg, a quencher of e). The MB solution, with an initial concentration of 5 mg/L in a volume of 100 mL, underwent a similar procedure to the previously described photocatalytic measurements [25].

The procedure employed to assess the durability of the catalyst involved several steps. After each catalytic run, the catalyst was separated from the aqueous solution through centrifugation, subjected to repeated washing with deionized water and ethanol, and subsequently dried at 80 °C overnight. Following this, all recycling tests were performed under consistent conditions. To evaluate the structural stability, a powder X-ray diffraction (XRD) analysis was conducted on the g-$C_3N_4$/CuO catalyst after five consecutive cycle runs.

## 3. Results and discussions

### 3.1. XRD patterns

X-ray powder diffraction (XRD) techniques were utilized to investigate the crystal structure and phases of g-C3N4, CuO, and the g-$C_3N_4$/CuO composite. Fig. 2 depicts the XRD patterns of the synthesized photocatalyst materials. The XRD pattern of pure g-C3N4 displayed a semi-crystalline nature with two distinct peaks. The prominent peak at 27°, corresponding to the (002) diffraction plane, is attributed to the inter-planar stacking of conjugated aromatic ring systems. This peak closely aligns with JCPDS card no. 87–1526. Furthermore, the faint peak at 13°, indexed to the (100) plane, is associated with the interlayer structural packing of tri-*s*-triazine [26,34].

In the sample consisting solely of CuO, two prominent peaks were observed in the X-ray diffraction analysis at 35.43° and 38.69°, which correspond to the JCPDS card no. 45–0937. These peaks confirm the monoclinic structure of CuO and correspond to the (002) and (111) diffraction planes, respectively. The XRD patterns further demonstrate the presence of the CuO phase in the g-C3N4/CuO composite. The results also indicate the substantial presence of both g-$C_3N_4$ and CuO in the g-$C_3N_4$/CuO nanocomposite, indicating the successful formation of the composite material.

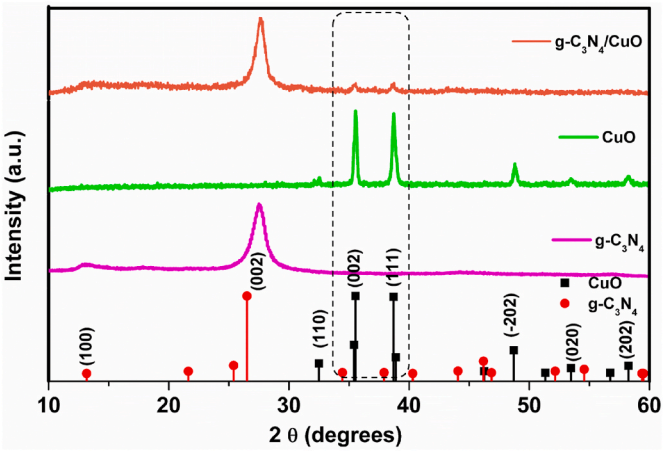


**Fig. 2.** XRD of g-$C_3N_4$, CuO and g-$C_3N_4$/CuO nanocomposite.

### 3.2. FE-SEM analysis

Fig. 3 depicts the FE-SEM images of g-$C_3N_4$, CuO, and g-$C_3N_4$/CuO nanomaterials. In Fig. 3a, the significant agglomeration, and larger particles with some curled structures present in g-C3N4 are visible. The lateral size of the g-C3N4 sheets is in the range of hundreds of nanometers. The FE-SEM micrograph of CuO in Fig. 3b clearly shows the needle and nanobelt morphology (lengths of approximately 100–200 nm and widths of around 10–30 nm). As illustrated in Fig. 3c, the g-$C_3N_4$/CuO nanocomposite displays both g-$C_3N_4$ and CuO morphologies, confirming the formation of the g-$C_3N_4$/CuO nanocomposite. This structure indicates that the interaction between g-$C_3N_4$ and CuO is more effective [35].

The crystalline characteristics of the CuO that was generated on the surface of the g-$C_3N_4$ is seen in HRTEM pictures and the selected area electron diffraction (SAED) pattern (Fig. 3d and e) of the active material. The selected area electron diffraction (SAED) pattern (Fig. 5d) can be indexed to the (110), (−111), (020), and (−113) crystal planes of monoclinic CuO, according to JCPDS No. 05–0661. This also demonstrated that the as-synthesized g-$C_3N_4$/CuO nanocomposites contained the CuO component, which was further confirmed by XPS results.

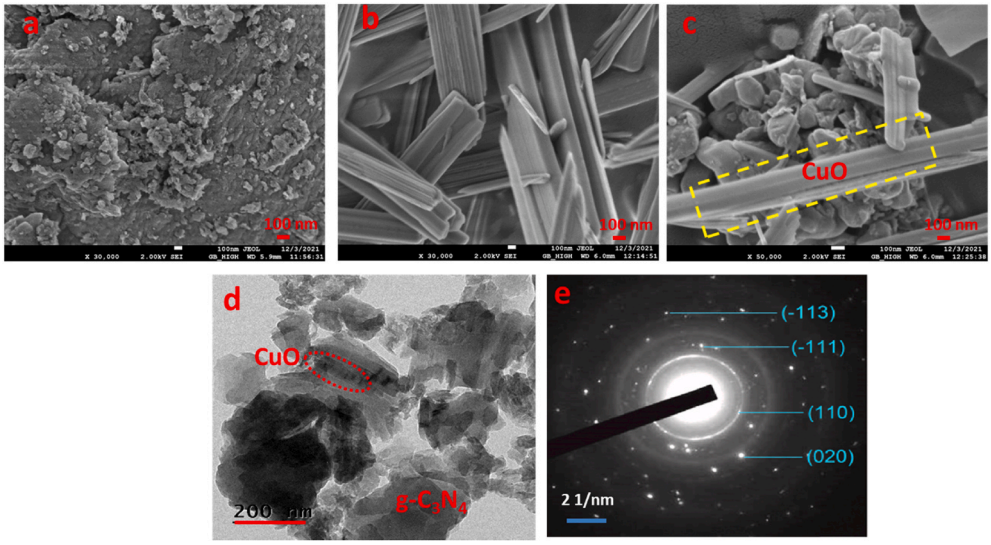


**Fig:3.** FE-SEM morphology of photocatalyst (a) g-$C_3N_4$ (b) CuO (c) g-$C_3N_4$/CuO (d) HR TEM and (e)SAED pattern of g-$C_3N_4$/CuO catalyst.

### 3.3. FTIR spectroscopy studies

The photocatalyst materials' FTIR spectra are depicted in Fig. 4. A noteworthy absorption peak at 806 $cm^{-1}$ in pure g-$C_3N_4$ is indicative of the out-of-plane skeletal bending vibration of the triazine unit-like C–N heterocycles. Furthermore, the usual C–N and C═N stretching modes are present in the band between 1200 and 1700 $cm^{-1}$. The stretching vibration of the Cu–O band, located at approximately 469 $cm^{-1}$, corresponds to the principal absorption peak in the CuO spectra. For the g-$C_3N_4$/CuO composite, peaks associated with the typical vibrations of the C–N and C═N bonds, as well as the stretching vibrations of the Cu–O bond, were observed. This outcome supports the production of g-$C_3N_4$/CuO nanocomposites and is consistent with the XRD findings.

### 3.4. UV vis – DRS analysis

The optical absorption characteristics of g-$C_3N_4$, CuO, and the g-$C_3N_4$/CuO nanocomposite were investigated using UV–Vis diffuse reflectance spectroscopy (DRS), as depicted in Fig. 5. The absorbance spectrum provides crucial insights into the electronic transitions and bandgap properties of these materials.

The absorbance spectrum of pure g-$C_3N_4$ (Fig. 5a) shows characteristic absorption peaks at approximately 245 nm and 324 nm. The peak at 245 nm corresponds to the π → π* electronic transition within the triazine aromatic rings, a structural feature of graphitic carbon nitride. The absorption at 324 nm is attributed to π → π* transitions within the conjugated heptazine rings, where lone pair electrons on the edge nitrogen (N) atoms contribute to the electronic excitation. The overall absorption edge of g-$C_3N_4$ extends into the visible range, indicating its semiconducting nature with a bandgap of approximately 2.72 eV, as determined from the Tauc plot (Fig. 5d).

For CuO (Fig. 5b), a broad absorption band is observed, extending from the UV to the visible region. This broad absorption is attributed to charge transfer transitions from oxygen 2p to copper 3d orbitals, characteristic of CuO's p-type semiconducting behavior. The estimated bandgap of CuO, calculated from the Tauc plot (Fig. 5e), is approximately 2.23 eV, confirming its strong visible-light absorption capabilities.

Upon the formation of the g-$C_3N_4$/CuO nanocomposite (Fig. 5c), a significant enhancement in absorbance is observed across the visible spectrum. Compared to pure g-$C_3N_4$, the composite exhibits a redshift in the absorption edge, suggesting an increased capacity for visible-light harvesting. The bandgap of the nanocomposite, estimated to be around 2.72 eV (Fig. 5f), is similar to that of g-$C_3N_4$. However, the improved absorption intensity indicates strong interfacial interactions between g-$C_3N_4$ and CuO, which may facilitate better charge separation and enhanced photocatalytic performance.

The spectral similarities between g-$C_3N_4$ and the g-$C_3N_4$/CuO nanocomposite arise due to the dominant optical response of g-$C_3N_4$ in the hybrid structure. However, the enhanced absorbance and extended absorption in the composite suggest that CuO contributes to light absorption and possibly alters charge carrier dynamics. The formation of heterojunctions between g-$C_3N_4$ and CuO likely improves charge transfer efficiency, reducing recombination and enhancing photocatalytic activity.

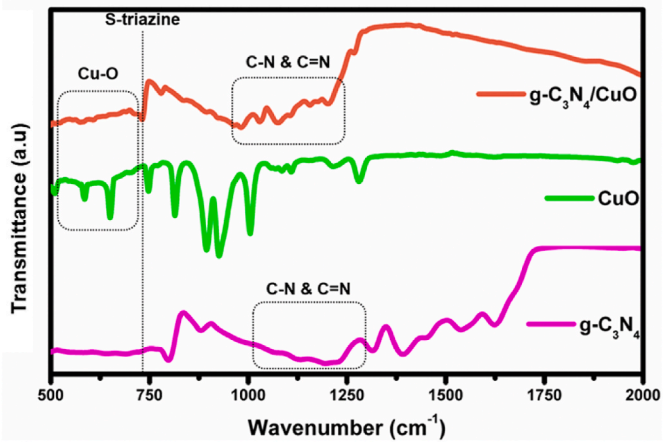


**Fig:4.** FTIR spectra of g-$C_3N_4$, CuO and g-$C_3N_4$/CuO catalyst.

### 3.5. PL and EIS analysis

To investigate the separation and transfer behaviors of free charge carriers and their impact on the photocatalytic performance of the catalysts, PL spectroscopy measurements were conducted. PL emissions arise due to the recombination of photo-generated electron-hole pairs, providing insights into charge separation efficiency. The PL emission spectra of pure g-$C_3N_4$, CuO, and g-$C_3N_4$/CuO nanocomposite are shown in Fig. 6a at room temperature. The central emission peak for g-$C_3N_4$ appears around 460 nm, corresponding to its intrinsic n-π* electronic transitions, with an energy band gap of 2.72 eV. The PL intensity of g-

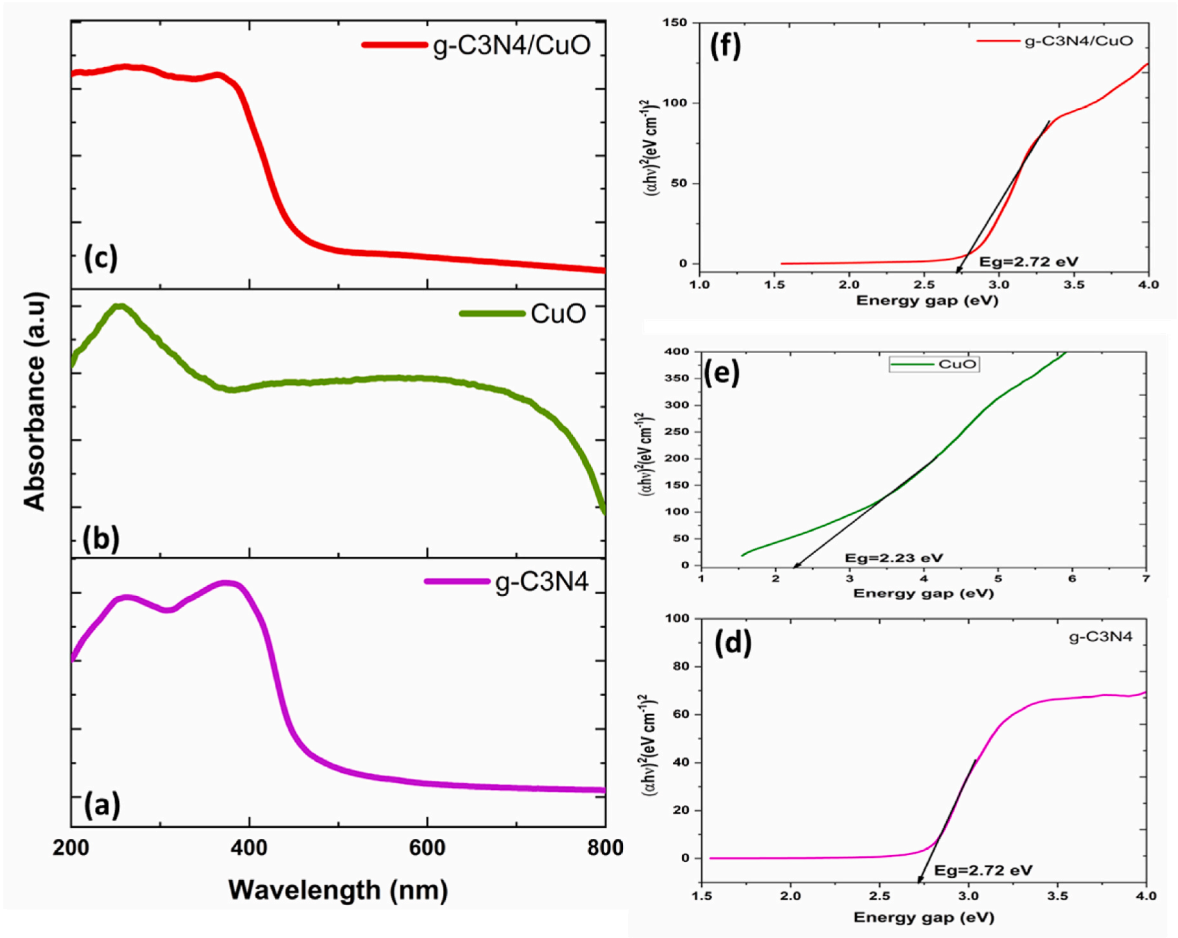


**Fig:5.** Uv–Vis Spectrum of (a) g-$C_3N_4$, (b) CuO (c) g-$C_3N_4$/CuO catalyst; and Energy gap calculation plot of (d) g-$C_3N_4$, (e) CuO (f) g-$C_3N_4$/CuO catalyst.

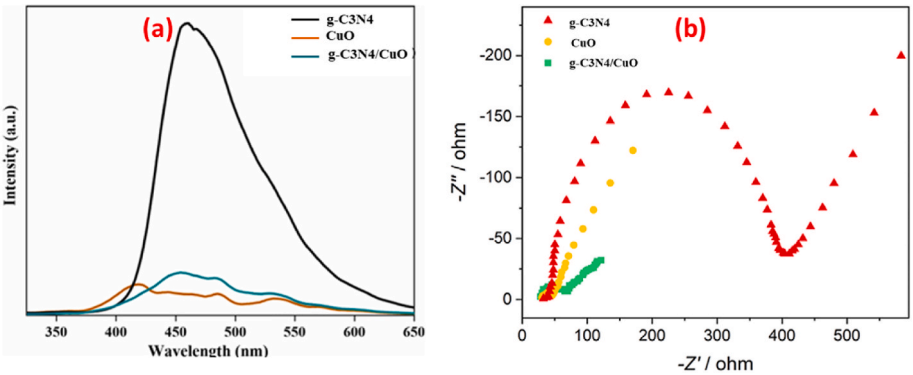


**Fig. 6.** (a)PL and (b) EIS plot of g-$C_3N_4$, CuO, and g-$C_3N_4$/CuO nanocomposite.

$C_3N_4$ is significantly higher, indicating a faster recombination rate of photogenerated electron-hole pairs, which typically reduces photocatalytic efficiency.

For pure CuO, a broad PL emission is observed, attributed to oxygen vacancies and surface defects, which play a role in charge trapping. The g-$C_3N_4$/CuO nanocomposite exhibits a significant reduction in PL intensity compared to pure g-$C_3N_4$. This suppression of recombination suggests an efficient transfer of photogenerated charge carriers between g-$C_3N_4$ and CuO, forming a heterojunction that enhances charge separation.

In the g-$C_3N_4$/CuO nanocomposite, photogenerated electrons migrate from the conduction band of g-$C_3N_4$ (−1.53 V vs NHE) to CuO (−0.27 V vs NHE) due to favorable band alignment. Simultaneously, holes transfer from the valence band of CuO (1.96 V vs NHE) to g-$C_3N_4$ (1.19 V vs NHE), further improving charge separation efficiency. This movement of charge carriers effectively reduces recombination, as supported by the observed lower PL intensity, thereby enhancing the photocatalytic performance of the g-$C_3N_4$/CuO nanocomposite. The formation of a heterojunction between g-$C_3N_4$ and CuO plays a critical role in facilitating charge transfer. The band alignment at the interface creates a built-in electric field that drives electrons from g-$C_3N_4$ to CuO and holes from CuO to g-$C_3N_4$, minimizing recombination losses. The observed reduction in PL intensity and the anticipated enhancement in photocatalytic activity confirm the synergistic effect of the g-$C_3N_4$/CuO

composite.

Electrochemical impedance spectroscopy (EIS) was used to evaluate the electron transfer resistance (Rct) of the prepared photocatalysts. The Nyquist plot (Fig. 6 (b)) presents the impedance response of g-$C_3N_4$, CuO, and g-$C_3N_4$/CuO, where the diameter of the semicircle corresponds to the interfacial charge transfer resistance. A smaller semicircle indicates lower resistance and more efficient charge separation. From the EIS results, pure g-$C_3N_4$ exhibits the highest charge transfer resistance, signifying slower electron transport and higher recombination rates. In contrast, CuO displays a lower Rct, suggesting improved electrical conductivity. The g-$C_3N_4$/CuO nanocomposite shows the smallest semicircle diameter, indicating significantly reduced charge transfer resistance compared to pure g-$C_3N_4$ and CuO. This enhanced charge separation efficiency in the composite system can be attributed to the formation of a heterojunction between g-$C_3N_4$ and CuO, which facilitates rapid electron transfer and reduces recombination losses.

The lower Rct values of the g-$C_3N_4$/CuO composite confirm its superior electron transport capability, which is essential for improving photocatalytic performance. The efficient charge transfer and reduced interfacial resistance in the heterostructure further support the enhanced photocatalytic activity observed in the g-$C_3N_4$/CuO system.

### 3.6. XPS analysis

Using X-ray Photoelectron Spectroscopy (XPS) to analyze the oxidation state of the components in the synthesized g-$C_3N_4$, CuO and g-$C_3N_4$/CuO nanoplates, as shown in Fig. 7a–c, revealed the presence of C, N, O, and Cu signals in the survey spectrum of the g-C3N4/CuO nanoplates, as shown in Fig. 8a-d. The resolved Cu 2p XPS spectrum in Fig. 8a displayed two major peaks at 933.9 and 954.1 eV, corresponding to Cu 2p3/2 and Cu 2p1/2, respectively. Furthermore, two satellite peaks indicating Cu2+ in CuO were also detected.

The resolved spectrum of O1s, as shown in Fig. 8b, displays a peak at 529.6 eV, which is attributed to O2 ions in the monoclinic lattice of CuO. Another peak located at 531.4 eV, indicating the C–O interaction and suggesting the interaction between CuO and g-C3N4 in the prepared g-$C_3N_4$/CuO nanoplates, is also visible in the fitted spectra of O1s.

The resolved C1s spectra in Fig. 8c exhibit two prominent peaks at 284.6 eV and 287.68 eV, corresponding to the sp2-hybridized C–N bond in the aromatic structure and the interaction between C–N and CuO.

The N1s signal at 399.5 eV in Fig. 6a indicates the existence of sp2-hybridized nitrogen atoms. The binding energies of oxygen, copper, nitrogen, and carbon reveal the formation of a g-$C_3N_4$/CuO heterostructure. This heterostructure is expected to exhibit enhanced charge carrier transfer and improved photocatalytic activity. According to the XPS spectra, the g-$C_3N_4$/CuO heterostructure comprises 20.18 % Cu, 32.52 % O, 28.22 % C, and 19.10 % N.

### 3.7. Degradation of organic pollutants MB

The study of the degradation of methylene blue (MB) in an aqueous solution under both dark and visible light irradiation served as a measure of the photocatalytic performance and provided valuable insight into the photocatalytic mechanism. A schematic illustration in Fig. 9 demonstrates the photocatalytic degradation of MB by g-$C_3N_4$/CuO nanocomposite materials. This schematic design was employed to showcase the efficiency of the g-$C_3N_4$/CuO photocatalyst, explaining the separation of electrons and holes, their reactivity, and the band-edge potential of the resulting photocatalyst. The valence band edge potential (VBE) and conduction band edge potential (CBE) of g-$C_3N_4$ were determined using the absolute electronegativity formula, as indicated below [36].

$$E_{VB} = \chi - E^e + 0.5\,E_g \tag{2}$$

$$E_{CB} = E_{VB} - E_g \tag{3}$$

where, $\chi$ is the absolute electronegativity of the semiconductor, $E_{CB}$ is the conduction band edge potential, $E_g$ is the band gap of the semiconductor, $E_{VB}$ is the valence band edge potential and Ee is the energy of free electrons on the hydrogen scale. The electronegativity value of g-$C_3N_4$ was 4.64 eV [37]. The conduction and valence band potentials of g-$C_3N_4$ are −1.53 and 1.19 V vs NHE, respectively. Similarly, the calculated band edge potentials for CuO are $E_{VB} = 1.96$ and $E_{CB} = -0.27$ V vs NHE. In Fig. 10a-c, the absorption spectrum of the methylene blue (MB) solution under visible light exposure is illustrated, clearly depicting the gradual decrease of the characteristic MB peak at 664 nm throughout the exposure period with a lesser blue shift. Catalysis with g-$C_3N_4$, CuO, and the g-$C_3N_4$/CuO nanocomposite resulted in significant concentration variations, indicating that the degradation was driven by the photocatalytic effects of the g-$C_3N_4$ and CuO catalysts.

The photocatalytic degradation efficiency was estimated using the formula $\eta = (1-C/C_0) \times 100$ %, where $C_0$ is the initial concentration, and C is the concentration after the degradation of the MB solution at each specific time. The estimated degradation efficiency values are shown in the $C/C_0$ graph in Fig. 10d. Remarkably, the g-$C_3N_4$/CuO sample achieved up to 98 % destruction of MB molecules within 40 min.

During the photocatalytic degradation process, when light shines on the supernatant solution, the g-$C_3N_4$ catalyst absorbs photon energy, allowing electrons in the valence band to move into the conduction band while the holes remain in the valence band. The separated electrons and holes actively contribute to the photocatalytic reaction, although some may recombine. The conduction band potential of g-$C_3N_4$/CuO was less favorable than the typical redox potential of $O_2/.O_2^-$ (−0.33 V), leading to the rapid transformation of dissolved oxygen molecules into superoxide anion radicals. These reactive oxygen species initiate photodegradation by damaging the MB molecules. Electrons in the conduction band break down organic pigments into $H_2O$ and $CO_2$, reducing $O_2$ to.

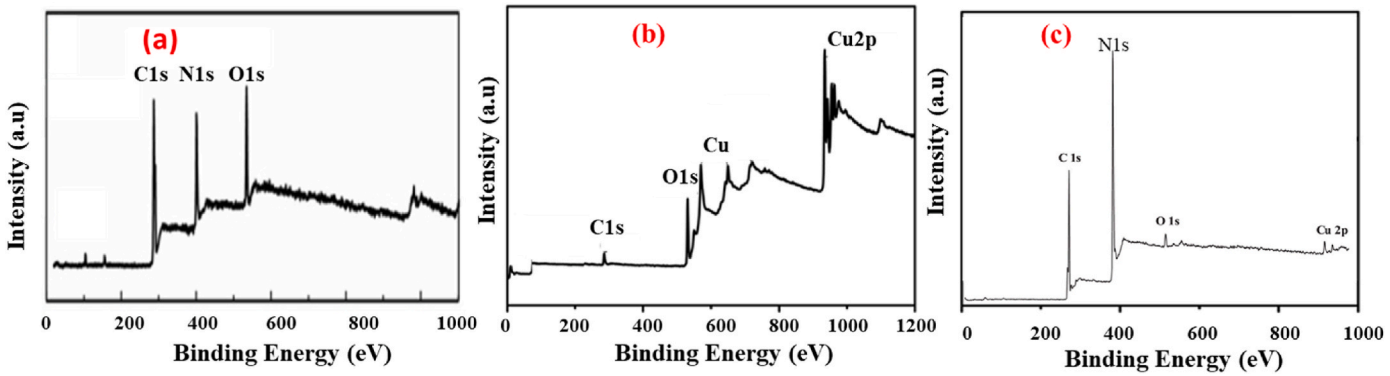


**Fig. 7.** XPS survey spectrum of the (a)g-C3N4, (b) CuO and (c) g-C3N4/CuO catalyst.

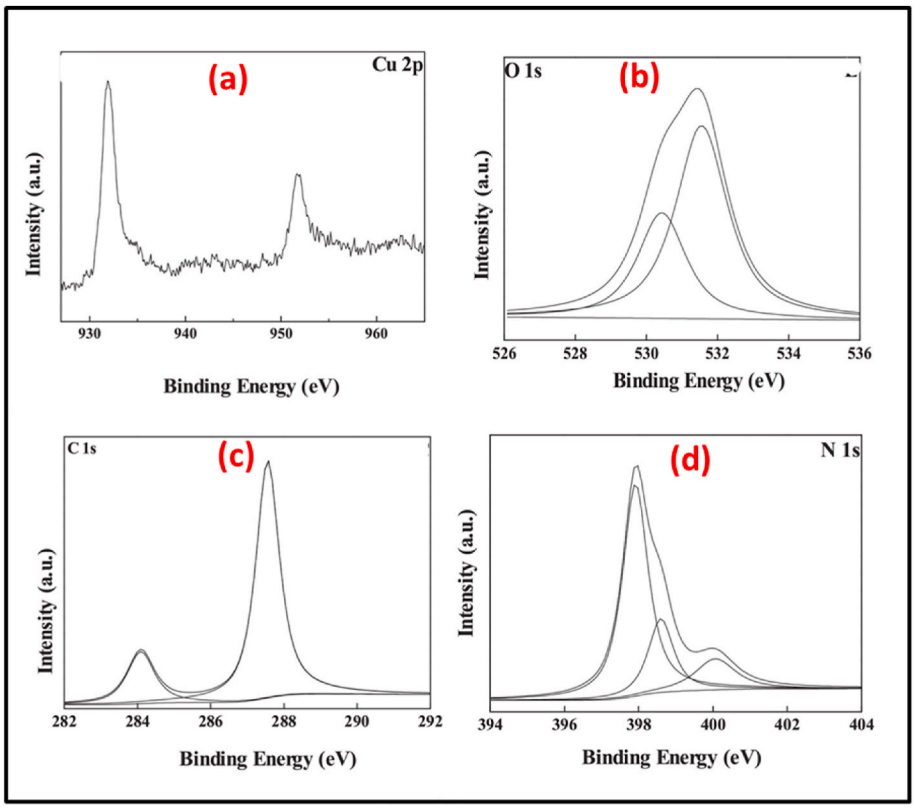


**Fig. 8.** XPS resolved (a)Cu2p, (b)O1s, (c)C1s and (d)N1s spectra.

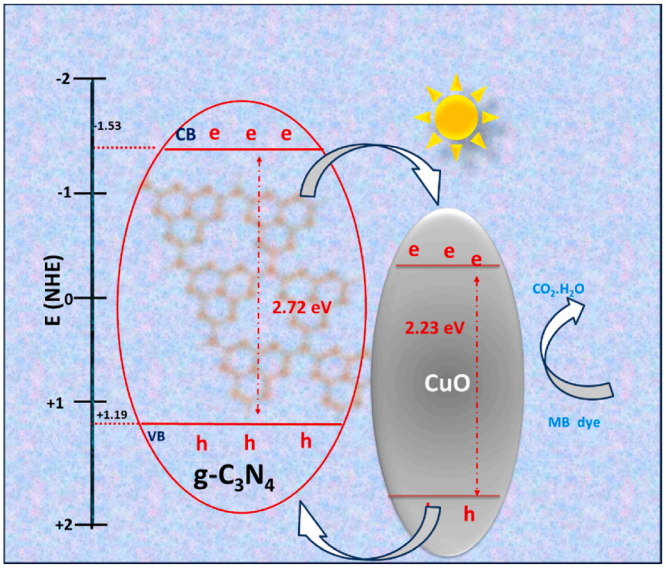


**Fig. 9.** Schematic illustration of g-$C_3N_4$/CuO photocatalyst mechanism under vis irradiation.

$O_2$- [38].

Fig. 10 illustrates the catalytic effects of all the generated samples on the degradation of the methylene blue (MB) solution, a process that results in the breakdown of chromophores responsible for MB's distinctive color of MB. To align with the experimental data, the first-order kinetic formula $\ln(C_0/C) = kt$ was used, where k is the first-order rate constant [39]. The calculated k values for g-$C_3N_4$, CuO, and the g-$C_3N_4$/CuO nanocomposite were 0.063, 0.068, and 0.072 $min^{-1}$, respectively.

The zeta potential values of all three catalysts were evaluated using a zeta potential analyzer (g-C3N4 = 41.6 mV, CuO = −46.8 mV, and g-$C_3N_4$/CuO = −47.9 mV) by dispersing the samples in deionized water. The surface of the g-$C_3N_4$/CuO nanocomposite exhibited more negative charges than the surfaces of pure g-$C_3N_4$ and CuO, enhancing the likelihood of interaction with molecules of the cationic dye MB. When visible light shines on the catalyst-mixed MB solution, a greater number of photogenerated electrons are produced, especially for the g-$C_3N_4$/CuO catalyst with a more negative surface potential (−47.9 mV). The increased negative surface charge of the g-C3N4/CuO nanocomposite compared to pristine g-C3N4 and CuO is attributed to the formation of the heterojunction. The strong electronic interactions between the two components lead to the redistribution of surface charges. Specifically, CuO donates electrons to g-C3N4, resulting in an overall more negative charge on the composite surface. This enhanced negative charge facilitates stronger interactions with the cationic MB molecules, increasing photocatalytic efficiency. The interaction between cationic dye molecules (MB) and more negative charges, coupled with the presence of photogenerated electrons, facilitated the rapid photocatalytic destruction of organic dye contaminants.

To understand the photocatalytic reaction mechanism during the degradation of the MB solution, trapping experiments with the g-$C_3N_4$/CuO catalyst were carried out. To detect h+, •OH, •O2-, and e, EDTA-2Na, IPA, BQ, and $AgNO_3$ were used as scavengers. It is clear from Fig. 10e that adding $AgNO_3$ greatly slows the deterioration of the MB solution (it deteriorates by only 70 % in 40 min). Other scavengers, such as EDTA-2Na, IPA, and BQ, on the other hand, had no discernible effect on the MB photodegradation procedure. As a result, the primary operational species in the photo-oxidation reaction are the photogenerated electrons.

The reusability of a catalyst is an essential factor for its practical application, particularly in large-scale enterprises where cost-effectiveness and sustainability are crucial considerations. A photocatalyst with high stability enables multiple uses, reducing the need for

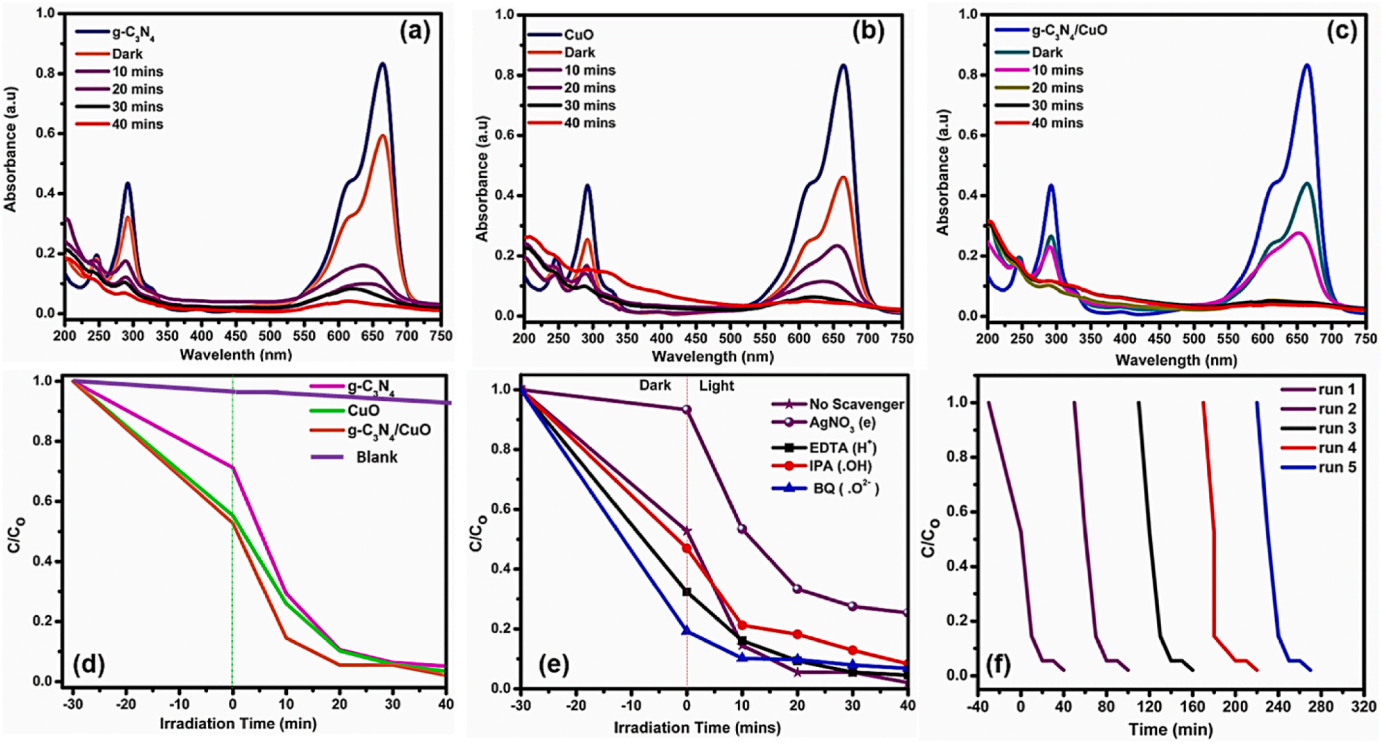


**Fig:10.** The absorbance spectra of MB solution with (a g-$C_3N_4$, (b) CuO, (c) g-$C_3N_4$/CuO, catalyst under visible light irradiation, (d) Photocatalytic degradation of MB solution for g-$C_3N_4$, CuO and g-$C_3N_4$/CuO photocatalysts, (e) MB photodegradation of g-$C_3N_4$/CuO catalyst with addition of scavengers (f) Photocatalytic degradation of MB solution in presence of g-$C_3N_4$/CuO catalyst under visible light irradiation with different cycles.

frequent replacement and making the contamination-removal process more economically viable. This is particularly important in industries or environmental remediation processes, where continuous and efficient removal of contaminants is required over an extended period. Therefore, the development of stable and reusable photocatalysts is vital for their successful implementation in practical applications and for addressing environmental challenges on a larger scale. The g-$C_3N_4$/CuO catalyst was employed repeatedly with the MB solution five times to assess its stability. Fig. 10f illustrates the results of the first and fifth iterations of the experiment.

After several cycles, the photocatalytic activity of the g-$C_3N_4$/CuO catalyst only slightly diminished, demonstrating the high level of stability of the catalyst. Therefore, the synthesized g-$C_3N_4$ photocatalyst can be utilized to purify water repeatedly. These outcomes are compared in Table 1 alongside previously published values.

## 4. Conclusions

In conclusion, the hydrothermal technique and simple thermal decomposition enabled successful fabrication of g-$C_3N_4$, CuO, and g-$C_3N_4$/CuO catalysts. Under visible-light irradiation, the synthesized g-C3N4/CuO catalyst showed significantly improved photocatalytic performance for MB degradation. More significantly, the g-$C_3N_4$/CuO catalyst degraded Mb (98 %) dye with a higher degradation efficiency than either the g-C3N4 catalyst or CuO catalyst. The g-$C_3N_4$/CuO catalyst demonstrated notable photocatalytic efficiency, which was attributed to enhanced photogenerated electrons during the degradation process. Additionally, its superior visible-light absorption was facilitated by its larger surface area and greater number of active sites. Even after five consecutive photocatalytic cycles, the g-$C_3N_4$/CuO catalyst maintained strong structural stability, indicating that the photocatalytic activity did not change. Overall, the current catalyst may be a strong

**Table 1**
Photocatalytic degradation using comparable photocatalysts across diverse reaction environments.

| S. No | Photocatalysts | Catalytic Degradation Dye (Catalyst dosage, dye dosage, dye concentration) | Catalytic environments | Rate of Catalytic activity | References |
|---|---|---|---|---|---|
| 1 | ZnO/g-$C_3N_4$ | methylene blue (100 mg, 100 ml, 50 mg/L | Visible light (500 W) | 88 %<br>180 min | [40] |
| 2 | g-$C_3N_4$/CuO | methylene blue (80 mg, 100 ml, 50 mg/L) | Visible light (500 W) | 94 %<br>100 min | [41] |
| 3 | CuO-SWCNT | methylene blue (150 mg, 100 ml,0.1 mg/L) | Natural sunlight | 97 %<br>120 min | [42] |
| 4 | $TiO_2$/g-$C_3N_4$ | Rhodamine B (50 mg, 100 mL, 10 mg/L) | Visible light (300 W) | 85 % (90 min) | [43] |
| 5 | Ag/g-$C_3N_4$ | Methyl orange (75 mg, 100 mL, 10 mg/L) | UV light (250 W) | 92 % (60 min) | [43] |
| 6 | $BiVO_4$/g-$C_3N_4$ | Rhodamine B (100 mg, 100 mL, 20 mg/L) | Visible light (300 W) | 89 % (120 min) | [44] |
| 7 | $Cu_2O$/g-$C_3N_4$ | Methylene blue (80 mg, 100 mL, 10 mg/L) | Visible light (450 W) | 96 % (80 min) | [45] |
| 8 | g-$C_3N_4$ | methylene blue (100 mg, 100 mL, 5 mg/L) | Visible light (400 W) | 94.4 %<br>40 min | **This work** |
| 9 | CuO | methylene blue (100 mg, 100 mL, 5 mg/L) | Visible light (400 W) | 96.3 %<br>40 min | **This work** |
| 10 | g-$C_3N_4$/CuO | methylene blue (100 mg, 100 mL, 5 mg/L) | Visible light (400 W) | 98 %<br>40 min | **This work** |

candidate for applications involving environmental protection.

## CRediT authorship contribution statement

**A. Muthuganesh:** Writing – original draft, Investigation, Formal analysis, Data curation, Conceptualization. **S. Mohamed Rafi:** Methodology, Investigation, Formal analysis, Conceptualization. **I. Davis Jacob:** Validation. **J.P. Soundranayagam:** Validation. **S. Surender:** Writing – review & editing, Writing – original draft, Validation, Methodology, Investigation, Formal analysis, Data curation, Conceptualization. **P. Elangovan:** Validation. **X. Helan Flora:** Writing – review & editing, Supervision.

## Data availability

No datasets were generated or analysed during the current study.

## Ethical approval

Not applicable.

## Funding statement

This research received no specific grant from any funding agency.

## Declaration of competing interest

The authors declare that they have no known competing financial interests or personal relationships that could have appeared to influence the work reported in this paper.

## Acknowledgements

The authors gratefully acknowledge the facilities provided by the Centre for Scientific and Applied Research, V.O.Chidambaram College, Tuticorin and Pachaiyappa's College, Chennai for conducting the experiments and characterizations.

## References

[1] M.I. Khan, et al., Green Synthesis of Magnesium Oxide Nanoparticles Using Dalbergia Sissoo Extract for Photocatalytic Activity and Antibacterial Efficacy, vol. 10, 2020, pp. 2351–2364.
[2] K. Kumar, et al., Photocatalytic, optical and magnetic properties of Fe-doped ZnO nanoparticles prepared by chemical route, J. Alloys Compd. 588 (2014) 681–689.
[3] C.M.B. Neves, et al., Photodegradation of metoprolol using a porphyrin as photosensitizer under homogeneous and heterogeneous conditions, J. Hazard Mater. 370 (2019) 13–23.
[4] A. Bashir, et al., Removal of heavy metal ions from aqueous system by ion-exchange and biosorption methods, Environ. Chem. Lett. 17 (2) (2019) 729–754.
[5] W. Pronk, et al., Gravity-driven membrane filtration for water and wastewater treatment: a review, Water Res. 149 (2019) 553–565.
[6] K. Naseem, et al., A systematic study for removal of heavy metals from aqueous media using Sorghum bicolor: an efficient biosorbent, Water Sci. Technol. 77 (10) (2018) 2355–2368.
[7] S. Saghafi, et al., Evaluation of aerobic/anaerobic industrial wastewater treatment processes: the application of multi-criteria decision analysis 38 (5) (2019) 13166.
[8] M.I. Din, et al., Biogenic scale up synthesis of ZnO nano-flowers with superior nano-photocatalytic performance, Inorganic Nano Metal Chem. 50 (8) (2020) 613–619.
[9] L. Yue, et al., Synthesis of efficient S-scheme heterostructures composed of BiPO(4) and KNbO(3) for photocatalytic N(2) fixation and water purification, Langmuir 40 (9) (2024) 4953–4965.
[10] J. Luo, et al., In suit constructing S-scheme FeOOH/MgIn2S4 heterojunction with boosted interfacial charge separation and redox activity for efficiently eliminating antibiotic pollutant, Chemosphere 298 (2022) 134297.
[11] S. Sarangapany, K. Mohanty. Facile Green Synthesis of Ag@ gC 3 N 4 for Enhanced Photocatalytic and Catalytic Degradation of Organic Pollutant vol. 32, 2021, pp. 585–592.
[12] N. Sutanto, et al., Heterojunction catalysts gC 3 N 4/-3ZnO-c-Zn 2 Ti 3 O 8 with highly enhanced visible-light-driven photocatalytic activity 93 (2020) 354–370.
[13] X. Han, et al., WO3/g-C3N4 two-dimensional composites for visible-light driven photocatalytic hydrogen production 43 (10) (2018) 4845–4855.
[14] M.B. Tahir, et al., Nanostructured-based WO3 photocatalysts: recent development, activity enhancement, perspectives and applications for wastewater treatment, Int. J. Environ. Sci. Technol. 14 (11) (2017) 2519–2542.
[15] K. Wang, et al., Harnessing zinc stannate for sustainable energy and environment solutions: advances in photocatalytic, piezocatalytic, and piezo-photocatalytic technologies, Nano Energy 133 (2025) 110518.
[16] K. Wang, Y. He, Recent advances in metal titanate-based piezocatalysts: enhancing catalytic performance through improved piezoelectric properties and regulated carrier transport, Chin. J. Catal. 61 (2024) 111–134.
[17] X. Ren, et al., Enhanced piezocatalytic RhB degradation with ZnSnO3 Nanocube-modified Bi4Ti3O12 composite catalyst by harnessing ultrasonic energy, J. Environ. Manag. 370 (2024) 122776.
[18] X. Zhou, et al., Synergistic effect of phosphorus doping and MoS2 co-catalysts on g-C3N4 photocatalysts for enhanced solar water splitting, J. Mater. Sci. Technol. 158 (2023) 171–179.
[19] X. Ma, et al., Construction of Netlike 3D Z-Scheme Photoelectrodes with Improved Photocatalytic Performance Based on G-C3n4 Nanosheets Modified TiO2 Nanobelt-Tubes, vol. 226, 2020 115844.
[20] H.Y. Hafeez, et al., Construction of ternary hybrid layered reduced graphene oxide supported g-C3N4-TiO2 nanocomposite and its photocatalytic hydrogen production activity 43 (8) (2018) 3892–3904.
[21] Y. Xian, et al., MoB2 modified g-C3N4: a Schottky junction with enhanced interfacial redox activity and charge separation for efficient photocatalytic H2 evolution, Separ. Purif. Technol. 345 (2024) 127337.
[22] D. Mohanta, M. Ahmaruzzaman, Facile fabrication of novel Fe(3)O(4)-SnO(2)-gC (3)N(4) ternary nanocomposites and their photocatalytic properties towards the degradation of carbofuran, Chemosphere 285 (2021) 131395.
[23] Y. Li, et al., 2D g-C3N4 for advancement of photo-generated carrier dynamics: status and challenges, Mater. Today 41 (2020) 270–303.
[24] G. Mamba, A.K. Mishra, Graphitic carbon nitride (g-C3N4) nanocomposites: a new and exciting generation of visible light driven photocatalysts for environmental pollution remediation, Appl. Catal. B Environ. 198 (2016) 347–377.
[25] R. Zhang, et al., Enhanced photocatalytic activity and optical response mechanism of porous graphitic carbon nitride (g-C3N4) nanosheets, Mater. Res. Bull. 140 (2021) 111263.
[26] Y. Huang, et al., Synthesis of CuO/g-C(3)N(4) composites, and their application to voltammetric sensing of glucose and dopamine, Mikrochim. Acta 186 (1) (2018) 10.
[27] M. Pourmadadi, et al., Two-dimensional graphitic carbon nitride (g-C3N4) nanosheets and their derivatives for diagnosis and detection applications 13 (4) (2022) 204.
[28] C. Zhao, et al., One-step preparation of novel Bi-Bi2O3/CdWO4 Z-scheme heterojunctions with enhanced performance in photocatalytic NH3 synthesis, J. Alloys Compd. 968 (2023) 171956.
[29] C. Zhao, et al., Bi4O5Br2 nanoflower and CdWO4 nanorod heterojunctions for photocatalytic synthesis of ammonia, ACS Appl. Nano Mater. 6 (17) (2023) 15709–15720.
[30] M. Hassanpour, et al., Microwave synthesis of CuO/NiO magnetic nanocomposites and its application in photo-degradation of methyl orange 27 (2016) 2718–2727.
[31] S.J. Moniz, J.J.C. Tang, Charge Transfer and Photocatalytic Activity in CuO/TiO2 Nanoparticle Heterojunctions Synthesised through a Rapid, One-Pot, Microwave Solvothermal Route, ChemCatChem 7 (11) (2015) 1659–1667.
[32] N. Zhou, et al., One-pot Fast Synthesis of Leaf-like CuO Nanostructures and CuO/Ag Microspheres with Photocatalytic Application, vol. 12, 2017 1750035, 03.
[33] M. Guo, et al., Highly Active and Recyclable CuO/ZnO as Photocatalyst for Transesterification of Waste Cooking Oil to Biodiesel and the Kinetics, vol. 315, 2022 123254.
[34] C. Qin, et al., CuO-ZnO hetero-junctions decorated graphitic carbon nitride hybrid nanocomposite: hydrothermal synthesis and ethanol gas sensing application, J. Alloys Compd. 770 (2019) 972–980.
[35] J. Kavil, et al., One-pot synthesis of g-C3N4/MnO2 and g-C3N4/SnO2 hybrid nanocomposites for supercapacitor applications, Sustain. Energy Fuels 2 (10) (2018) 2244–2251.
[36] Y.R. Girish, et al., Facile and rapid synthesis of solar-driven TiO2/g-C3N4 heterostructure photocatalysts for enhanced photocatalytic activity, J. Sci.: Adv. Mater. Device 7 (2) (2022) 100419.
[37] J. Li, et al., Fabrication of g-C3N4/TiO2 composite photocatalyst with extended absorption wavelength range and enhanced photocatalytic performance, J. Photochem. Photobiol. Chem. 317 (2016) 151–160.
[38] N. Chidhambaram, K. Ravichandran, Single step transformation of urea into metal-free g-C3N4 nanoflakes for visible light photocatalytic applications, Mater. Lett. 207 (2017) 44–48.
[39] M.R.S. Nivetha, et al., Construction of SnO(2)/g-C(3)N(4) an effective nanocomposite for photocatalytic degradation of amoxicillin and pharmaceutical effluent, Environ. Res. 209 (2022) 112809.
[40] R.C. Ngullie, et al., Synthesis and characterization of efficient ZnO/g-C3N4 nanocomposites photocatalyst for photocatalytic degradation of methylene blue 10 (5) (2020) 500.
[41] T.P. Vijayakumar, et al., Hydrothermal synthesis of CuO/g-C3N4 nanosheets for visible-light driven photodegradation of methylene blue, Diam. Relat. Mater. 121 (2022) 108735.
[42] K.P. Sapkota, et al., Enhanced visible-light photocatalysis of nanocomposites of copper oxide and single-walled carbon nanotubes for the degradation of methylene blue 10 (3) (2020) 297.
[43] N. Premalatha, P. Rajalakshmi, L.R. Miranda, Photocatalytic degradation of Rhodamine B over TiO2/g-C3N4 and immobilized TiO2/g-C3N4 on stainless steel

wire gauze under UV and visible light: a detailed kinetic analysis and mechanism of degradation, React. Kinet. Mech. Catal. 135 (2) (2022) 1031–1046.

[44] Q. Liu, et al., Synthesis of Ag3PO4/Ag/g-C3N4 composite for enhanced photocatalytic degradation of methyl orange, Molecules 28 (2023), https://doi.org/10.3390/molecules28166082.

[45] S. Kumaravel, et al., Highly efficient solar-light-active Ag-decorated g-C3N4 composite photocatalysts for the degradation of methyl orange dye, Micromachines 14 (2023), https://doi.org/10.3390/mi14071454.